

Direct measurement of dopant distribution in an individual vapour–liquid–solid nanowire

Daniel E. Perea, Eric R. Hemesath, Edwin J. Schwalbach, Jessica L. Lensch-Falk, Peter W. Voorhees and Lincoln J. Lauhon*

Semiconductor nanowires show promise for many device applications^{1–3}, but controlled doping with electronic and magnetic impurities remains an important challenge^{4–8}. Limitations on dopant incorporation have been identified in nanocrystals⁹, raising concerns about the prospects for doping nanostructures^{9,10}. Progress has been hindered by the lack of a method to quantify the dopant distribution in single nanostructures. Recently, we showed that atom probe tomography can be used to determine the composition of isolated nanowires^{11,12}. Here, we report the first direct measurements of dopant concentrations in arbitrary regions of individual nanowires. We find that differences in precursor decomposition rates between the liquid catalyst and solid nanowire surface give rise to a heavily doped shell surrounding an underdoped core. We also present a thermodynamic model that relates liquid and solid compositions to dopant fluxes.

The vapour–liquid–solid (VLS)¹³ growth process is one of the most widely used nanowire growth methods, because it offers excellent control of nanowire size¹⁴ and composition¹⁵. In VLS growth, a vapour-phase precursor catalytically decomposes at a metal nanoparticle surface, forming a supersaturated eutectic liquid. The solid crystalline nanowire grows by precipitation from the liquid catalyst particle. In the present work, gold nanoparticles were used to synthesize germanium nanowires from a GeH₄ precursor. The incorporation of intentional impurities into nanowires, or doping, is usually accomplished by introducing dopant precursor gases during synthesis^{1,4,5,7}, but the concentration and distribution of dopants has not previously been determined, precluding quantitative assessments of dopant incorporation rates and obscuring a fundamental understanding of the origins of the electronic properties of nanowires. Recently, we used pulsed-laser atom probe tomography to measure the composition of nanowires^{11,12} and determine the concentration of dilute impurities¹⁶ with atomic-scale resolution and part-per-million sensitivity. Here, we focus on atom probe studies of dopant atom distributions in VLS-grown germanium nanowires to quantify the doping efficiency and identify the processes influencing the incorporation rate.

The application of atom probe tomography to nanowires^{12,16} and the generation of quantitative tomographic reconstructions¹⁷ have been described elsewhere. The scanning electron microscopy (SEM) image in Fig. 1a establishes that the reconstruction in Fig. 1b is accurate in morphology and scale. The tapered structure results from uncatalysed decomposition of GeH₄ on the sides of the nanowire during growth^{18,19}. Such reactions can be eliminated by the appropriate choice of reactor conditions²⁰, but the taper is beneficial for pulsed-laser atom probe analysis because it increases thermal conductivity and mechanical strength¹⁶. Distinct Ge(111) planes, oriented perpendicular to the growth direction (Fig. 1c), are unambiguous evidence of atomic resolution and provide an

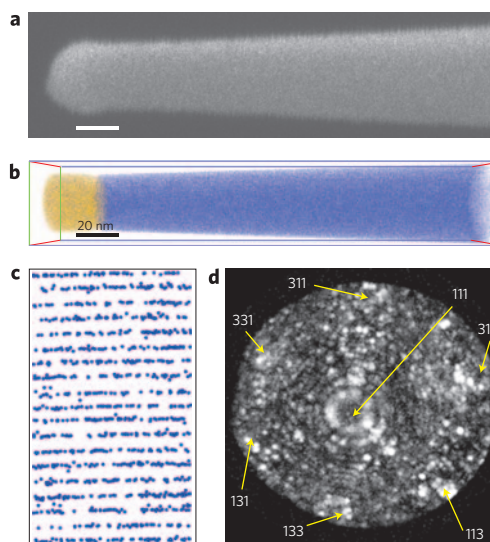


Figure 1 | Atomically resolved three-dimensional reconstruction of a germanium nanowire. **a**, SEM image for comparison. **b**, Tomographic reconstruction showing gold (yellow) and germanium (blue) atoms; phosphorus atoms not shown. Scale bars, 20 nm. **c**, Slice of reconstruction showing Ge(111) planes normal to nanowire growth direction. The plane spacing is 0.32 ± 0.01 nm, and the image is rotated 90° with respect to **a**. **d**, Indexed FIM image of the germanium nanowire shown in **a** and reconstructed in **b**. The nanowire shown here was grown at 380°C and a ratio of 1:1,000 of PH_3 : GeH_4 .

internal distance calibration along the analysis direction. A quantitative calibration of radial distances was achieved through atomically resolved analysis of field ion microscopy (FIM) images (Fig. 1d) taken immediately following atom probe analysis. Concentric rings of surface atoms (bright spots) are observed around the central $\langle 111 \rangle$ pole and surrounding higher-index poles where discrete low-index atomic planes intersect the surface of the specimen. The $\langle 111 \rangle$ pole defines the centre of the nanowire and provides the reference point for mapping radial variations in composition and doping.

The distribution of phosphorus dopants is radially inhomogeneous (Fig. 2a), with a heavily doped shell surrounding a core of much lower phosphorus concentration. The core region consists of germanium crystallized out of the Au–Ge(l) nanocatalyst, whereas the shell results from uncatalysed surface growth. A high concentration of oxygen atoms around the perimeter (Fig. 2b) indicates the presence of a native oxide that formed upon removal from the growth chamber and establishes the extent of the electrically conductive material. The dopant distribution throughout the length of the

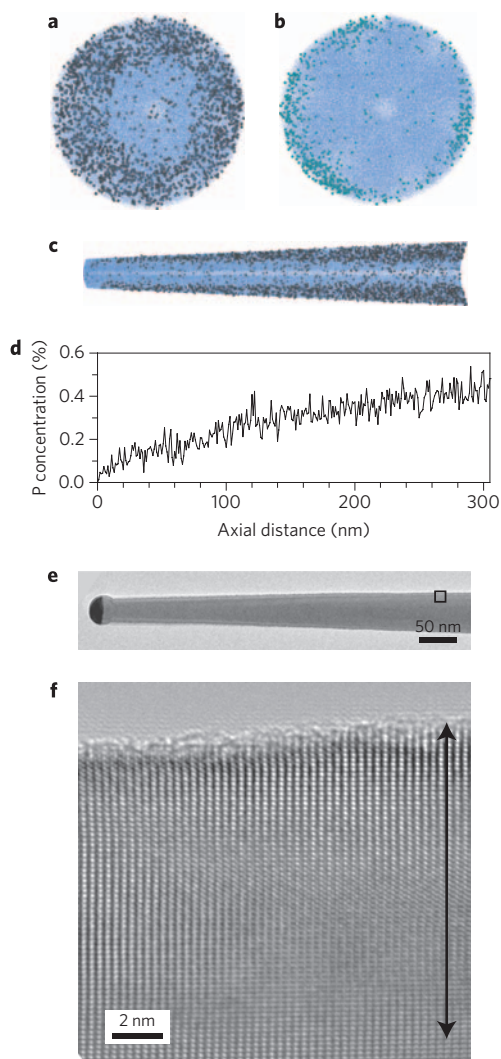


Figure 2 | Distribution of dopant atoms. **a,b**, End-on view (43 nm in diameter) of nanowire highlighting the distribution of phosphorus (**a**, grey spheres) and oxygen (**b**, light blue spheres) in germanium (blue dots). The nanowire was grown under the same conditions as the one shown in Fig. 1. **c**, Side view of nanowire cross-section (2 nm thick) aligned with **d**. **d**, Average phosphorus concentration along the growth axis. **e**, Bright-field TEM image of phosphorus-doped germanium nanowire. Scale bar, 50 nm. **f**, High-resolution bright-field TEM image of phosphorus-doped shell region inside the box in **e**. The large black arrow (12 nm) illustrates the extent of the phosphorus-doped shell. Scale bar, 2 nm.

analysed volume is revealed in a 2-nm-thick slice from the reconstruction taken parallel to the growth direction (Fig. 2c). The radially averaged dopant concentration increases monotonically with increasing distance from the wire tip (Fig. 2d), consistent with preferential phosphorus incorporation onto the surface of the nanowire during growth. This implies that the resistivity of a germanium nanowire grown using the VLS process may vary both radially and axially if uncatyalsed surface reactions occur during growth. Indeed, a recent report of the electrical characteristics of phosphorus-doped germanium nanowires suggested that the observed n-type behaviour originated from a heavily doped shell, and the core doping was proposed to be electrically insignificant compared to that of the shell⁶. In contrast to this earlier work, we are able to directly measure the dopant concentrations in arbitrary regions of the material. At a $\text{PH}_3 : \text{GeH}_4$ flow ratio of 1 : 1,000, which would give a phosphorus concentration of $4.4 \times 10^{19} \text{ cm}^{-3}$ for stoichiometric incorporation, the core is

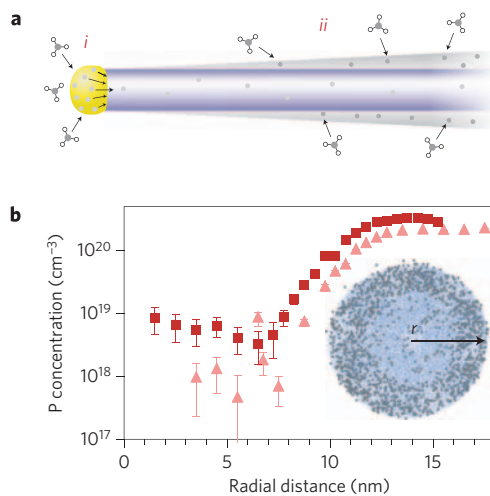


Figure 3 | Dopant incorporation pathways and distribution. **a**, Schematic representation of dopant incorporation pathways via the catalyst (*i*) and surface decomposition (*ii*). **b**, Radial plot of phosphorus concentration for germanium nanowires grown at 380 °C and $\text{PH}_3 : \text{GeH}_4$ ratios of 1 : 1,000 (triangles) and 1 : 500 (squares). The inset shows the path along which the concentration was measured.

substantially underdoped ($9 \times 10^{17} \pm 3 \times 10^{17} \text{ cm}^{-3}$), and the shell is substantially overdoped ($1.95 \times 10^{20} \pm 0.02 \times 10^{20} \text{ cm}^{-3}$). Values for four different nanowires from the same growth run are plotted in Supplementary Fig. S1 to show the consistency of this discrepancy. Observation of P_2 ions in the mass spectrum of the shell (see Supplementary Fig. S2) may indicate some degree of electrically inactive dimer formation, although we note that the resolution of the reconstruction is insufficient to determine electrical activity. Transmission electron microscopy (TEM) measurements confirm that the doped shell is epitaxial (Fig. 2e, f). This is consistent with the incorporation of some fraction of substitutional phosphorus atoms, as the formation of electrically inactive phosphorus–phosphorus dimers suppresses the epitaxial growth of phosphorus-doped germanium thin films²¹.

Although quantitative dopant distributions are important to the understanding and control of electrical properties, they also enable a detailed consideration of dopant incorporation pathways and rates. During VLS growth, dopants can be incorporated into the core through the catalyst and onto the surface by uncatyalsed decomposition, shown schematically in Fig. 3a as pathways *i* and *ii*, respectively¹⁸. Given the higher surface doping, one should also consider whether dopants diffuse from the nanowire surface into the core during growth. The region of uniform doping within the core (Fig. 3b) is much greater than the expected thermal diffusion length of $\sim 1 \text{ nm}$ (ref. 22), leading us to conclude that the phosphorus in the core results exclusively from incorporation through the catalyst droplet. The phosphorus core concentration of $9 \times 10^{17} \pm 3 \times 10^{17} \text{ cm}^{-3}$ is well below the solubility of substitutional phosphorus in germanium, which is $\sim 2 \times 10^{20} \text{ cm}^{-3}$ at the growth temperature of 380 °C (ref. 23), suggesting that phosphorus incorporation has not been limited by the absolute solubility of phosphorus in germanium. This is qualitatively confirmed by observing that a doubling of the PH_3 flow rate increases both the core and shell concentrations (Fig. 3b), indicating that the dopant level can be controlled. Quantitatively, averages of three to four nanowires for each growth condition indicate that the core concentration increases from $1.3 \times 10^{18} \pm 0.2 \times 10^{18} \text{ cm}^{-3}$ to $2.1 \times 10^{18} \pm 0.2 \times 10^{18} \text{ cm}^{-3}$ (Table 1).

The large discrepancy between the core and shell doping levels reflects differences in the underlying reaction kinetics for the two

Table 1 | Average phosphorus, oxygen and gold concentrations within the nanowire core. All concentrations are in units of $1 \times 10^{18} \text{ cm}^{-3}$. Gold concentrations are displayed as upper bounds because no gold signal was detected above the background.

	380 °C and 1:1,000	380 °C and 1:500	300 °C and 1:500
Phosphorus	1.3 ± 0.2	2.1 ± 0.2	2.3 ± 0.3
Oxygen	0.5 ± 0.2	0.3 ± 0.1	1.5 ± 0.1
Gold	<0.2	<0.2	<0.2

distinct pathways. The uncatalysed surface growth is not essentially different from conventional chemical vapour deposition processes²¹ in which the phosphorus concentration is determined by the rates of dissociative chemisorption of GeH_4 and PH_3 . Under our growth conditions, the phosphorus concentration follows a simple Arrhenius relationship (see Supplementary Fig. S3). We conclude that thermally activated PH_3 decomposition occurs more readily than GeH_4 decomposition on the nanowire surface, with the caveat that intermediate species resulting from gas-phase reactions may also be present. We can express this observation quantitatively by first noting that the vapour–solid (V–S) growth rate of the shell (V_{VS}) is $\sim 20 \text{ nm min}^{-1}$ and that the phosphorus concentration in the shell is $\sim 3 \times 10^{20} \text{ cm}^{-3}$ for the 1:500 growth. Assuming that phosphorus is dilute, conservation of mass implies that $V_{\text{VS}} = -J_{\text{Ge}}^{\text{VS}}/\rho_{\text{Ge}}$, where $J_{\text{Ge}}^{\text{VS}}$ is the germanium flux resulting from GeH_4 decomposition and ρ_{Ge} is the density of germanium. Using the ideal gas law to estimate the GeH_4 flux at the surface $J_{\text{GeH}_4}^{\text{V}}$, we find that $J_{\text{Ge}}^{\text{VS}} \cong 6 \times 10^{-6} J_{\text{GeH}_4}^{\text{V}}$. In other words, GeH_4 undergoes dissociative chemisorption in six out of every 10^6 encounters with the surface. We estimate that PH_3 undergoes dissociative chemisorption in 14 out of every 10^6 encounters, confirming the relative enhancement in decomposition rate.

A similar analysis can be applied to the catalyst-mediated VLS growth. In steady-state growth, and neglecting for the moment evaporation of germanium or phosphorus into the vapour phase, the integrated flux of germanium atoms across the liquid–solid (L–S) interface must equal the integrated flux of germanium atoms across the vapour–liquid (V–L) interface. As each precursor species contains one germanium or one phosphorus atom, the rate of germanium (phosphorus) atom transfer across the L–S interface must therefore equal the rate of GeH_4 (PH_3) decomposition at the V–L interface. We thereby estimate that GeH_4 undergoes dissociative chemisorption 120 out of every 10^6 encounters, which is a 20-fold increase over the dissociation rate on the nanowire surface. Indeed, germanium nanowire growth is observed in part because the catalyst induces preferential decomposition of GeH_4 at the nanowire tip. Surprisingly, PH_3 undergoes dissociative chemisorption in only two out of every 10^6 encounters, which represents a seven-fold decrease compared with the uncatalysed V–S growth on the nanowire surface. We note that the PH_3 dissociation rate is an underestimate if the chemical potential of the phosphorus in the liquid is high enough to produce evaporation. In such a circumstance, we might expect to see a diameter-dependent phosphorus concentration due to the Gibbs–Thomson effect, in which the surface energy of the droplet leads to an increasing chemical potential at small diameters. We do not observe systematic variations in core dopant concentration with diameter or temperature (Fig. 4). The comparable core doping levels at the two growth temperatures and the lack of a Gibbs–Thomson effect suggest, but do not prove, that phosphorus evaporation is insubstantial. Although one might conclude that the different kinetics of the two distinct PH_3 decomposition pathways produces the lower core doping rate, it is worth considering the thermodynamic factors that influence the kinetics to develop a more thorough description of the VLS doping process.

The thermodynamic driving forces for incorporation at the V–L interface and crystallization at the L–S interface are related to the difference in the appropriate thermodynamic energy function on either side of the respective interfaces. Schmidt and colleagues²⁴

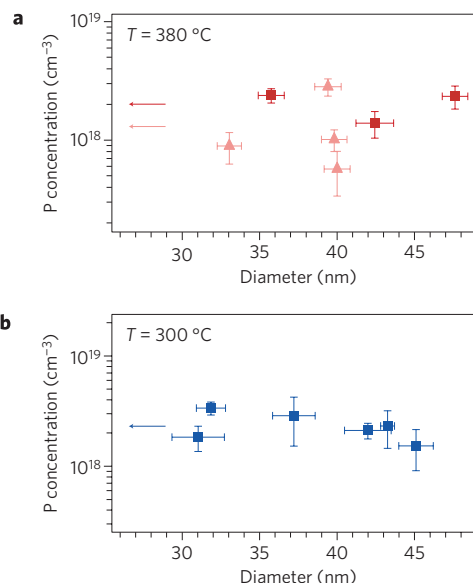


Figure 4 | Core phosphorus concentration versus temperature and precursor ratio. a, Wires grown at 380 °C and PH_3 : GeH_4 ratios of 1:1,000 (triangles) and 1:500 (squares). **b**, Wires grown at 300 °C and a PH_3 : GeH_4 ratio of 1:500. The coloured arrows indicate the average concentration for the respectively coloured data sets.

have proposed a thermodynamic model of nanowire growth in binary systems (for example, gold–germanium) in which the incorporation and crystallization rates are expressed in terms of chemical potential differences without considering changes in chemical potential due to decomposition. In the steady state, incorporation and crystallization rates are equal, and small changes in the chemical potential lead to changes in the growth rate. In binary systems, the equilibrium composition is fixed by the phase diagram, so the composition of the droplet cannot change with flux provided diffusion is fast and local equilibrium holds at the L–S interface, which is a good assumption at these very low growth rates²⁵. In ternary systems, however, the assumption of local equilibrium at the growth interface does not uniquely determine the compositions of the liquid and solid²⁶. As will be shown below, the fluxes influence the local equilibrium composition of the liquid at the L–S interface, changing the chemical potentials of the phosphorus and germanium atoms in the liquid, which, in turn, affect the precursor decomposition and incorporation rates into the liquid according to the model of Schmidt and colleagues²⁴. In other words, the build-up of phosphorus in the droplet in the presence of a flux may influence the decomposition of PH_3 through changes in the chemical potential of phosphorus in the liquid. In this context, it is not appropriate to speak of a single rate-limiting step in doping.

We have explicitly connected the doping kinetics with the solution thermodynamics by developing a one-dimensional steady-state model that relates the compositions in the liquid and solid, X^{L} and X^{S} , to the fluxes of germanium and phosphorus atoms (J_{Ge} , J_{P}) through the liquid during growth. To illustrate the unique

aspects of nanowire growth from a ternary liquid, the liquid is treated as an ideal ternary solution and the solid as a dilute binary alloy of phosphorus in germanium because of the extremely limited gold solid solubility. Additional details are provided in the Methods. We find that the liquid compositions X_P^l and X_{Ge}^l at the L–S interface are given by

$$X_P^l = \frac{\hat{X}_P^l J_P}{\hat{X}_P^s J_{Ge}} \quad (1)$$

$$X_{Ge}^l = \frac{\hat{X}_{Ge}^l}{\hat{X}_{Ge}^s} \left(1 - \frac{J_P}{J_{Ge}} \right) \quad (2)$$

where \hat{X}_P^s , \hat{X}_{Ge}^s and \hat{X}_P^l , \hat{X}_{Ge}^l are the equilibrium concentrations of the solid and liquid, respectively. Previously, we have shown that the variation of composition within the liquid that accompanies diffusion is extremely small, and thus equations (1) and (2) give the composition of the entire liquid²⁷. The model reveals that the presence of the fluxes induces changes in the liquid compositions, and therefore the liquid chemical potentials, with respect to their reference state values. This is a consequence of the fact that the liquid is a ternary alloy, and not because of a deviation from equilibrium at the L–S interface. In stark contrast, the liquid chemical potentials in a binary system are determined by the liquid composition only, indicating that quantitative models of VLS nanowire doping should consider the solution thermodynamics of the ternary liquid and solid along with the dynamics of mass flow in the liquid phase.

In support of the model presented here, we note that equation (2) predicts that the germanium composition in the liquid, and therefore the growth rate, will exhibit a dependence on the phosphorus flux. To test this prediction, we grew nanowires with a $PH_3 : GeH_4$ ratio of 1 : 172, and observed a decrease in growth rate of 16% relative to the intrinsic nanowire growth rate with the same GeH_4 flux. Despite this confirmation, we do not suggest that this thermodynamic model explains the VLS-defined core doping level. On the contrary, distinct barriers for GeH_4 and PH_3 decomposition on the liquid probably influence the core doping level. Instead, the model identifies thermodynamic quantities that can influence the doping rates and highlights that for the case of doping from a ternary liquid it may not be appropriate to speak of a single rate-limiting process. We should also point out recent progress in understanding nanowire doping through V–S reactions on nanowires⁸. In particular, dopant precursor species have been shown to have profound effects on nanowire morphology when the dominant incorporation pathway is via surface reactions²⁸. It is also worth noting that earlier authors have pursued intentional surface doping when VLS doping was not efficient or otherwise contraindicated²⁰.

Given the influence of the L–S interface on dopant incorporation in the solid as described above, alternative dopants and catalysts represent an important area of research for the development of nanowire-based device technology. In this context, one should also consider that unintentional impurities can affect the carrier concentration. The VLS process uses a metal catalyst, introducing the possibility of metal contamination²⁹, and gold in particular is known to be a deep trap/acceptor and can act as a recombination centre. No gold is detected in the nanowires (Table 1), indicating that gold plays a negligible role in determining the majority carrier type. Nanowire growth often takes place in moderate vacuum, and oxygen, which is a donor species in germanium³⁰, may be incorporated from the reactor background gases. The summary data in Table 1 show oxygen concentrations in these nanowires of the same magnitude as phosphorus concentrations, suggesting that oxygen may contribute to ambipolar conduction and/or compensation in intrinsic and lightly doped p-type

germanium nanowires. The possibility that unknown impurities may compensate intentional dopants should be considered when making inferences about intentional doping levels based on electrical measurements alone. Considering the quantitative information and insights on doping mechanisms presented here, we expect that correlated atom probe tomography and electrical measurements on nanowires will further the development of nanowire device technology in the near future.

Methods

Phosphorus-doped germanium nanowires were synthesized with GeH_4 and PH_3 (200 ppm in helium) with hydrogen and helium co-flows within a hot-walled CVD reactor at a total pressure of 50 torr. Flow rates in $cm^3 s^{-1}$ at standard temperature and pressure were 2, 20 and 28 for GeH_4 , helium and hydrogen, respectively. Pulsed-laser atom probe tomography was performed using a local electrode atom probe (LEAP) 3000X Si from Imago Scientific Instruments housed at the Northwestern University Center for Atom Probe Tomography (NUCAPT). Analysis was performed at a base pressure of $< 8 \times 10^{-11}$ torr and temperature of 60 K. Laser pulses of 10 ps width from a 532 nm laser were focused on the nanowire tip. A pulse frequency of 100 kHz, pulse energies of 0.02–0.1 nJ, and evaporation rates of 0.2–0.5% were used. Nanowire sample preparation for atom probe analysis has been described elsewhere¹⁶.

Tomographic reconstructions were generated and analysed using IVAS v3.0. SEM was used to directly estimate the nanowire taper angle and initial tip radius from single images (Fig. 1a). FIM was used to estimate the image compression factor (ICF)¹⁷. The ICF, shank angle and initial tip radius were used to produce a preliminary reconstruction volume from which the Ge(111) interplanar spacing could be measured as a function of axial distance from the tip. The shank angle and initial tip radius were systematically varied to obtain a constant Ge(111) plane spacing of 0.32 ± 0.1 nm throughout the entire reconstruction length (Fig. 1c). The final shank angle and tip radius agreed with values obtained from SEM analysis within experimental error.

In our thermodynamic model of nanowire doping, the liquid is treated as an ideal ternary solution and the solid as a dilute binary alloy of phosphorus in germanium because of the extremely limited gold solid solubility. The reference state is described by the following conditions. First, the solid and liquid are in global equilibrium, so the growth rate is zero. Second, the solid with phosphorus composition X_P^s , is in equilibrium with a liquid of composition X_P^l , X_{Ge}^l given by the ternary phase diagram for the system. During growth, we assume that the germanium and phosphorus fluxes induce sufficiently small composition changes at the L–S interface that the chemical potentials of germanium and phosphorus in the solid and liquid may be linearized about the reference state; the extension to large deviations is straightforward. Local equilibrium is maintained during growth; that is, the chemical potentials μ_{Ge} and μ_P do not change across this interface. The above assumptions give the expressions

$$\frac{X_P^l}{X_P^s} = \frac{\hat{X}_P^l}{\hat{X}_P^s} \quad (3)$$

$$\frac{X_{Ge}^l}{X_{Ge}^s} = \frac{\hat{X}_{Ge}^l}{\hat{X}_{Ge}^s} \quad (4)$$

where the compositions during growth are on the left-hand side of the equalities. Equations (3) and (4) imply that the nanowire core doping can be controlled provided that the concentrations of phosphorus in the liquid and solid are below the equilibrium solubilities. This is confirmed by our observation that the core doping level can be controlled by the PH_3 flow. Mass conservation of both germanium and phosphorus at the L–S interface, as used earlier to determine dissociation rates, provides two more equations,

$$X_P^s = \frac{J_P}{J_{Ge} + J_P} \cong \frac{J_P}{J_{Ge}} \quad (5)$$

$$X_{Ge}^s = 1 - \frac{J_P}{J_{Ge} + J_P} \cong 1 - \frac{J_P}{J_{Ge}} \quad (6)$$

where J_{Ge} and J_P are the atomic fluxes of germanium and phosphorus through the liquid, respectively, and we have assumed that $0 < J_P \ll J_{Ge}$. Substitution of equation (5) into equation (3) and equation (6) into equation (4) gives equations (1) and (2) above, respectively.

Received 31 December 2008; accepted 17 February 2009;
published online 29 March 2009

References

1. Cui, Y. & Lieber, C. M. Functional nanoscale electronic devices assembled using silicon nanowire building blocks. *Science* **291**, 851–853 (2001).
2. Thelander, C. *et al.* Nanowire-based one-dimensional electronics. *Mater. Today* **9**, 28–35 (2006).
3. Lu, W. & Lieber, C. M. Nanoelectronics from the bottom up. *Nature Mater.* **6**, 841–850 (2007).
4. Cui, Y., Duan, X. F., Hu, J. T. & Lieber, C. M. Doping and electrical transport in silicon nanowires. *J. Phys. Chem. B* **104**, 5213–5216 (2000).
5. Gudiksen, M. S. *et al.* Growth of nanowire superlattice structures for nanoscale photonics and electronics. *Nature* **415**, 617–620 (2002).
6. Tutuc, E., Chu, J. O., Ott, J. A. & Guha, S. Doping of germanium nanowires grown in presence of PH_3 . *Appl. Phys. Lett.* **89**, 263101 (2006).
7. Lew, K. K. *et al.* Structural and electrical properties of trimethylboron-doped silicon nanowires. *Appl. Phys. Lett.* **85**, 3101–3103 (2004).
8. Stamplecoskie, K. G., Ju, L., Farvid, S. S. & Radovanovic, P. V. General control of transition-metal-doped GaN nanowire growth: Toward understanding the mechanism of dopant incorporation. *Nano Lett.* **8**, 2674–2681 (2008).
9. Erwin, S. C. *et al.* Doping semiconductor nanocrystals. *Nature* **436**, 91–94 (2005).
10. Norris, D. J., Efros, A. L. & Erwin, S. C. Doped nanocrystals. *Science* **319**, 1776–1779 (2008).
11. Perea, D. E. *et al.* Three-dimensional nanoscale composition mapping of semiconductor nanowires. *Nano Lett.* **6**, 181–185 (2006).
12. Perea, D. E. *et al.* Composition analysis of single semiconductor nanowires using pulsed-laser atom probe tomography. *Appl. Phys. A* **85**, 271–275 (2006).
13. Wagner, R. S. & Ellis, W. C. Vapor–liquid–solid mechanism of single crystal growth. *Appl. Phys. Lett.* **4**, 89–90 (1964).
14. Cui, Y. *et al.* Diameter-controlled synthesis of single-crystal silicon nanowires. *Appl. Phys. Lett.* **78**, 2214–2216 (2001).
15. Duan, X. F. & Lieber, C. M. General synthesis of compound semiconductor nanowires. *Adv. Mater.* **12**, 298–302 (2000).
16. Perea, D. E. *et al.* Tomographic analysis of dilute impurities in semiconductor nanostructures. *J. Solid State Chem.* **181**, 1642–1649 (2008).
17. Gault, B. *et al.* Estimation of the reconstruction parameters for atom probe tomography. *Microsc. Microanal.* **14**, 296–305 (2008).
18. Lauhon, L. J., Gudiksen, M. S., Wang, C. L. & Lieber, C. M. Epitaxial core–shell and core–multishell nanowire heterostructures. *Nature* **420**, 57–61 (2002).
19. Kamins, T. I., Li, X. & Williams, R. S. Growth and structure of chemically vapor deposited Ge nanowires on Si substrates. *Nano Lett.* **4**, 503–506 (2004).
20. Greytak, A. B., Lauhon, L. J., Gudiksen, M. S. & Lieber, C. M. Growth and transport properties of complementary germanium nanowire field-effect transistors. *Appl. Phys. Lett.* **84**, 4176–4178 (2004).
21. Jang, S. M., Liao, K. & Reif, R. Phosphorus doping of epitaxial Si and $\text{Si}_{1-x}\text{Ge}_x$ at very low pressure. *Appl. Phys. Lett.* **63**, 1675–1677 (1993).
22. Sodervall, U. & Friesel, M. Diffusion of silicon and phosphorus into germanium as studied by secondary ion mass spectrometry. *Defect. Diffus. Forum* **143**, 1053–1058 (1997).
23. Fistul, V. I. *et al.* Solubility and segregation of electrically active phosphorus in Ge. *Inorg. Mater.* **11**, 457–459 (1975).
24. Schmidt, V., Senz, S. & Gosele, U. Diameter dependence of the growth velocity of silicon nanowires synthesized via the vapor–liquid–solid mechanism. *Phys. Rev. B* **75**, 045335 (2007).
25. Aziz, M. J. Model for solute redistribution during rapid solidification. *J. Appl. Phys.* **53**, 1158–1168 (1982).
26. Coates, D. E. Diffusion-controlled precipitate growth in ternary systems 1. *Metall. Trans.* **3**, 1203–1212 (1972).
27. Roper, S. M. *et al.* Steady growth of nanowires via the vapor–liquid–solid method. *J. Appl. Phys.* **102**, 034304 (2007).
28. Radovanovic, P. V., Stamplecoskie, K. G. & Pautler, B. G. Dopant ion concentration dependence of growth and faceting of manganese-doped GaN nanowires. *J. Am. Chem. Soc.* **129**, 10980–10981 (2007).
29. Allen, J. E. *et al.* High-resolution detection of Au catalyst atoms in Si nanowires. *Nature Nanotech.* **3**, 168–173 (2008).
30. Clauws, P. Oxygen related defects in germanium. *Mater. Sci. Eng. B* **36**, 213–220 (1996).

Acknowledgements

This work was supported by the Office of Naval Research and the National Science Foundation through the CAREER and NIRT programs. D.E.P. acknowledges the support of a Ford Foundation fellowship, J.L.L. acknowledges the support of a NSF Graduate Fellowship, E.J.S. acknowledges support of a National Defense Science and Engineering Graduate Fellowship, and L.J.L. acknowledges support of an Alfred P. Sloan Research Fellowship. We acknowledge the NUANCE and NUCAPT facilities for the use of instrumentation and D. Isheim for useful discussions.

Author contributions

D.E.P. performed the atom probe experiments and data analysis. E.R.H. and J.L.F. synthesized the nanowires. E.R.H. performed TEM analysis. E.J.S. and P.W.V. developed the growth model. L.J.L. coordinated the design and execution of the experiments. D.E.P. and L.J.L. co-wrote the manuscript. All authors discussed the results and commented on the manuscript.

Additional information

Supplementary Information accompanies this paper at www.nature.com/naturenanotechnology. Reprints and permission information is available online at <http://npg.nature.com/reprintsandpermissions/>. Correspondence and requests for materials should be addressed to L.J.L.